



Cu current collector with binder-free lithiophilic nanowire coating for high energy density lithium metal batteries

Syed Abdul Ahad, Esther Adegoke, KEVIN M. RYAN, HUGH GEANEY

Publication date

19-02-2023

Published in

Small 2023, 2207902

Licence

This work is made available under the [CC BY-NC-SA 4.0](#) licence and should only be used in accordance with that licence. For more information on the specific terms, consult the repository record for this item.

Document Version

1

Citation for this work (HarvardUL)

Abdul Ahad, S., Adegoke, E., RYAN, K.M. and GEANEY, H. (2023) 'Cu current collector with binder-free lithiophilic nanowire coating for high energy density lithium metal batteries', available: <https://doi.org/10.34961/researchrepository-ul.22683085.v1>.

This work was downloaded from the University of Limerick research repository.

For more information on this work, the University of Limerick research repository or to report an issue, you can contact the repository administrators at ir@ul.ie. If you feel that this work breaches copyright, please provide details and we will remove access to the work immediately while we investigate your claim.



Spray Coating Experiments: Setups and Methodologies



**The latest eBook from
Advanced Optical Metrology.
Download for free.**

Spray Coating Experiments: Setups and Methodologies, is the third in our Thin Films eBook series. This publication provides an introduction to spray coating, three article digests from Wiley Online Library and the latest news about Evident's Image of the Year Award 2022.

Wiley in collaboration with Evident, are committed to bridging the gap between fundamental research and industrial applications in the field of optical metrology. We strive to do this by collecting and organizing existing information, making it more accessible and useful for researchers and practitioners alike.

EVIDENT
OLYMPUS

WILEY

Cu Current Collector with Binder-Free Lithiophilic Nanowire Coating for High Energy Density Lithium Metal Batteries

Syed Abdul Ahad, Temilade Esther Adegoke, Kevin M. Ryan, and Hugh Geaney*

Despite significant efforts to fabricate high energy density (ED) lithium (Li) metal anodes, problems such as dendrite formation and the need for excess Li (leading to low N/P ratios) have hampered Li metal battery (LMB) development. Here, the use of germanium (Ge) nanowires (NWs) directly grown on copper (Cu) substrates (Cu-Ge) to induce lithiophilicity and subsequently guide Li ions for uniform Li metal deposition/stripping during electrochemical cycling is reported. The NW morphology along with the formation of the $\text{Li}_{15}\text{Ge}_4$ phase promotes uniform Li-ion flux and fast charge kinetic, resulting in the Cu-Ge substrate demonstrating low nucleation overpotentials of 10 mV (four times lower than planar Cu) and high Columbic efficiency (CE) efficiency during Li plating/stripping. Within a full-cell configuration, the Cu-Ge@Li – NMC cell delivered a 63.6% weight reduction at the anode level compared to a standard graphite-based anode, with impressive capacity retention and average CE of over 86.5% and 99.2% respectively. The Cu-Ge anodes are also paired with high specific capacity sulfur (S) cathodes, further demonstrating the benefits of developing surface-modified lithiophilic Cu current collectors, which can easily be integrated at the industrial scale.

1. Introduction

Li metal anodes have gained much interest recently, due to the approaching performance threshold of Li-ion batteries (LIBs).^[1,2] To exceed the practically achievable EDs of LIBs (250–280 Wh Kg⁻¹) using standard graphite anodes (372 mAh g⁻¹), a significant technological leap to Li metal batteries (LMBs) is widely expected.^[3–5] Li metal is highly attractive among the catalog of potential anode materials due to its low density (0.53 g cm⁻³), high theoretical capacity (3860 mAh g⁻¹), and low electrochemical potential (–3.04 V vs standard hydrogen electrode (SHE)).^[6–8] With such features, Li metal can be paired with high-capacity cathode materials such as sulfur (S) (2500 Wh Kg⁻¹) and O₂ (3350 Wh Kg⁻¹) along with existing


high-voltage cathode materials (e.g., NMC) to deliver beyond the state of the art EDs.^[9–11] However, the adoption of LMBs as a replacement for LIBs has been slow due to key mechanistic hurdles.^[12] These problems include unstable solid electrolyte interface (SEI) formation due to electrolyte incompatibility with the reactive Li surface,^[13,14] uneven Li deposition due to non-uniform surface current density,^[15] and inactive “dead” Li formation, causing severe Columbic efficiency (CE) losses during cycling.^[16,17] In extreme cases, the uneven Li plating/stripping during charge-discharge processes causes catastrophic dendrite formation, piercing the separator and causing short-circuits; a prime reason for the infamous battery fires in electronic devices and electric vehicles (EVs).^[18,19]

Several noteworthy strategies have been devised to overcome the issues linked to LMB development such as liquid electrolyte modification with various

performance tuning additives,^[20–22] concentrated electrolyte formulations,^[23–25] and the use of solid-state electrolytes (SSE).^[26,27] These approaches partly mitigate the issue of unstable SEI formation, however, uneven Li deposition with subsequent dendrite formation poses a major challenge towards LMBs commercialization.^[6] To overcome dendrite formation, strategies including the development of Li-containing foreign hosts (i.e., carbon scaffolds, metallic foams) with high surface-area features^[28–30] (porous networks, NWs, etc.) coated with lithiophilic materials^[31–34] (elemental, oxides, sulfides, etc.) have been reported. These ingenious strategies have enabled smooth Li deposition/stripping during electrochemical cycling, leading to enhanced cycling stability compared to planar Li foils.

To enable genuine cell-level ED enhancements in future LMBs, the use of low-weight current collectors (CCs) and minimization of superfluous mass is a critical requirement, however, this aspect has been largely ignored to date in the literature.^[35] Given that commercial LIBs use planar Cu foil CCs at the anode due to their lightweight, low density, and cost, it is prudent to continue research on the development of modified planar Cu CCs for LMBs.^[35–37] Unfortunately, Cu is a highly lithiophobic material that promotes uneven Li deposition and dendrite formation without surface modification.^[38] Several strategies have been devised to impart lithiophilicity by incorporating Ag, Cu_xO, ZnO, NiO, graphene, etc. architectures on Cu.^[39–43] These architectures promote uniform Li-ion flux, by creating a lithiophilic surface, thereby promoting uniform Li

S. A. Ahad, T. E. Adegoke, K. M. Ryan, H. Geaney
Department of Chemical Sciences and Bernal Institute
University of Limerick
Limerick V94 T9PX, Ireland
E-mail: hugh.geaney@ul.ie

 The ORCID identification number(s) for the author(s) of this article can be found under <https://doi.org/10.1002/smll.202207902>.

© 2023 The Authors. Small published by Wiley-VCH GmbH. This is an open access article under the terms of the Creative Commons Attribution License, which permits use, distribution and reproduction in any medium, provided the original work is properly cited.

DOI: 10.1002/smll.202207902

deposition.^[37] However, along with the development of lithiophilic planar Cu substrates with minimal synthesis steps, a conscious effort is required to limit the amount of deposited Li within these anodes, to maximize the ED of the LMB full cell.^[1,7]

In this study, we demonstrate the growth of Ge NWs on thin Cu foil as a lithiophilic host for Li anodes in LMBs. The Ge NWs grown on Cu foil (Cu-Ge) present several advantages including i) Ge NWs directly grown on Cu surface contain no “dead” weight from a binder or conductive agent which helps to improve the ED of the LMBs, ii) Ge is a highly lithiophilic material with high Li-ion diffusivity which helps to regulate the Li-ion flux during Li plating/stripping processes.^[44–47] iii) The dense NW morphology enhances the surface area of the substrate, which reduces the localized current density at the Cu-Ge substrate, thereby promoting uniform Li deposition.^[48,49] Moreover, our group has recently studied the lithiophilic effect of Ge (along with other materials, i.e., Si, SiGe alloy), figuring out that Li-Ge has high Li binding energy as compared to Li-Si alloy.^[50] With the stated advantages, nucleation overpotentials of as low as 10 mV were achieved when Li was plated on the Cu-Ge surface, which is four times lower than on a Cu substrate. The lithiophilicity of the Cu-Ge substrate promoted uniform Li deposition and enabled a significant anode weight saving of 63.6% compared to a benchmark graphite anode when paired with an NMC811 cathode. Additional testing with an S cathode confirmed the compatibility of the Cu-Ge current collector with high-specific capacity cathodes.

2. Results and Discussion

The synthesis route of Ge NWs grown on Cu foil (Cu-Ge) is illustrated in **Figure 1a**. It involves the use of a vapor-solid-solid (VSS) approach where the surface of the Cu foil acts as a seed layer for the growth of Ge NWs.^[51–53] After injection of diphenyl germane (DPG) at 450 °C, the thermal decomposition of the

organometallic germanium precursor initiates the growth of Ge NWs from a copper germinide (Cu₃Ge) seed. The whole reaction takes <5 min, resulting in the growth of highly dense Ge NWs firmly adhered to the Cu foil. These densely grown Ge NWs on Cu foil were then used directly as current collectors for LMBs (Figure S1, Supporting Information). The proposed mechanism of the guided Li deposition on Cu-Ge foil is illustrated in Figure 1b,c. With the presence of lithiophilic Ge NWs on Cu-Ge substrate, the local current density decreases due to the high surface area of the NW structure (as compared to planar Cu substrate) along with the high Li ion diffusion during lithiation of Ge to lithium germinide^[20,51,54,55] (Li₁₅Ge₄): 15Li⁺ + 4Ge + 15e⁻ → Li₁₅Ge₄. Further deposition of Li on Li₁₅Ge₄ NWs results in reduced nucleation overpotential of Li, thus promoting uniform Li deposition/stripping with no dendrite formation. In contrast, the planar Cu foil with low surface area and lithiophobic Cu surface, promotes non-uniform current density distribution, thereby giving rise to the formation of uneven Li deposits and subsequent dendrite formation during the plating process.

X-ray diffraction (XRD) analysis of Cu and Cu-Ge highlights the compositional changes after reaction with DPG for Ge NWs growth (**Figure 2a** and **Figure S2**, Supporting Information). Before the reaction, peaks from the Cu foil at 43.3°, 50.5°, and 74.2° correspond to the (111), (200), and (220) planes of Cu. After the reaction with DPG, several additional peaks appeared, among which diffraction peaks at 27.3°, 45.3°, and 53.7° corresponding to the (111), (220), and (311) crystallographic planes of Ge. Further, major peaks from Cu₃Ge at 43.08° and 45.1° corresponding to (020) and (012) can also be observed. The scanning electron microscopy (SEM) analysis shows the dense growth of Ge NWs over Cu foil (**Figure 2b** & inset, **Figure S3**, Supporting Information) with an average Ge NW diameter of 92.6 nm (**Figure S4**, Supporting Information). The cross-sectional SEM of the Cu-Ge sample shows the side view of Cu foil and the top view of Ge NWs grown over the Cu surface (**Figure 2c**). Corresponding energy dispersive spectroscopy (EDX) analysis

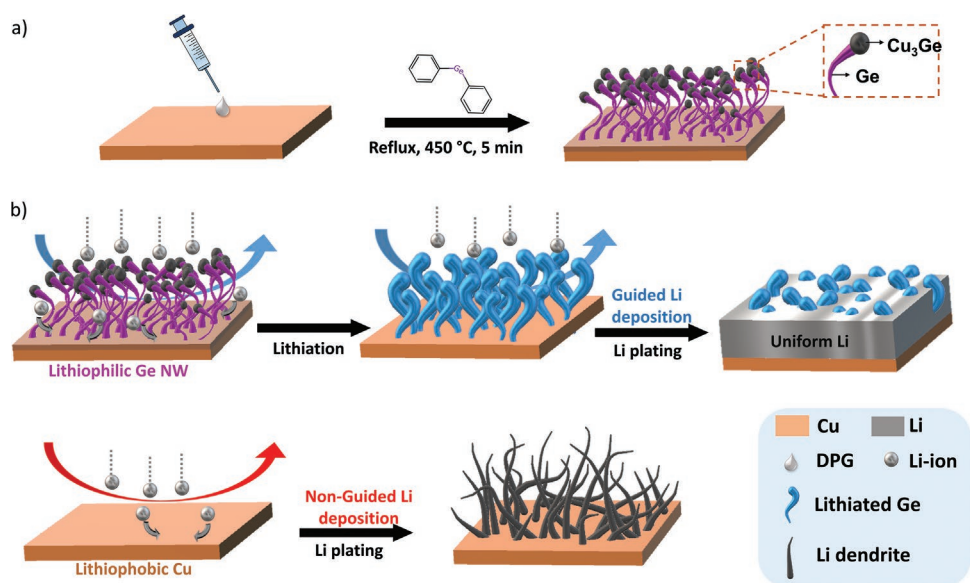


Figure 1. Schematic illustration of a) Ge NWs synthesis on Cu foil and b) Li plating behavior on Cu-Ge and Cu substrates.

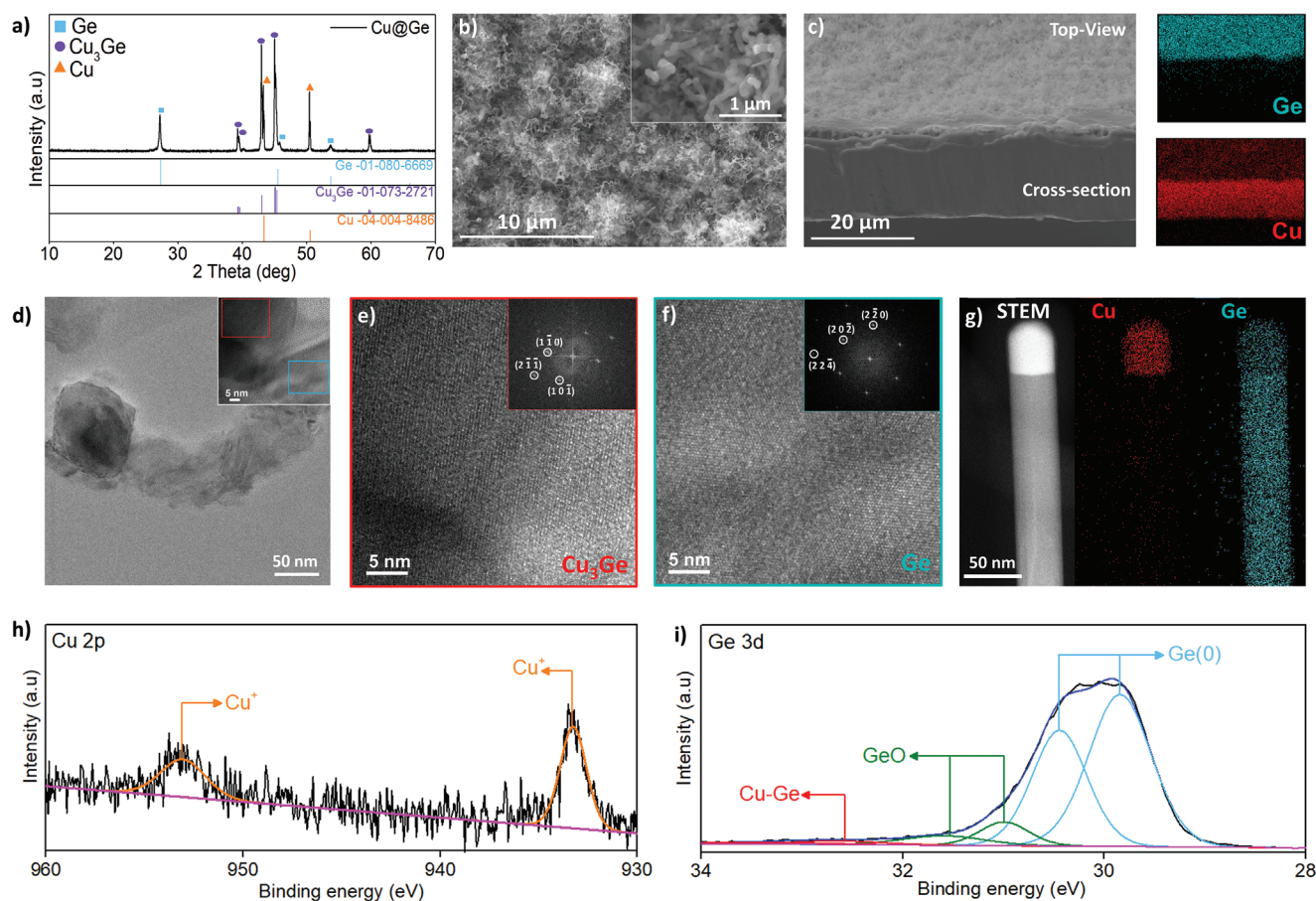


Figure 2. a) XRD analysis of Cu-Ge substrate. SEM analysis of b) Cu-Ge surface and c) cross-sectional surface along with EDX mapping of Ge (blue) and Cu (red). d–f) HRTEM images of Cu_3Ge seeded Ge NWs along with their corresponding FFTs. g) STEM images with corresponding EDX mapping of Cu_3Ge seed and Ge NW. h–i) Cu 2p and Ge 3d XPS core spectra of Cu-Ge substrate.

shows Cu signals concentrated at the cross-sectional side, while the Ge signals are concentrated at the surface of the Cu-Ge foil. The transmission electron microscopy (TEM) analysis of Ge NW (Figure 2d) shows a round Cu_3Ge seed attached to a Ge NW, which suggests the growth mechanism to be VSS since the reaction was carried out below the Cu/Ge eutectic temperature (i.e., 644 °C).^[56–58] The high-resolution images and corresponding FFT analysis of the marked region (Figure 2d-inset) of Cu_3Ge seed and Ge NW can be seen in Figure 2e,f. The images were taken down the [111] zone axis and the respective FFTs are indexed with planes $(1\bar{1}0)$, $(2\bar{1}\bar{1})$, and $(10\bar{1})$ for Cu_3Ge while $(2\bar{2}0)$, $(20\bar{2})$, and $(22\bar{4})$ for the Ge NW. Scanning TEM (STEM) analysis of Ge NW shows the Cu and Ge distribution along the NW length with STEM image clearly showing different contrast of seed and NW region (Figure 2h). The corresponding mapping shows Cu signals only concentrated in the Cu_3Ge seed region while Ge signals are concentrated in the NW region with relatively less concentration in the seed area. The XPS analysis further confirms the presence of Cu and Ge species in the Cu-Ge sample. The Cu 2p spectra show multiplet splitting peaks (Cu 2p_{3/2} and Cu 2p_{1/2}) corresponding to the Cu^+ (933.2 and 953.1 eV) species (Figure 2h), which can be associated with the Cu_3Ge phase. The Ge 3d spectra show various peaks, which correspond to Ge-Ge (29.8 eV), GeO (31 eV),

and Cu-Ge (32.5 eV) binding energy, appearing due to the presence of the Cu_3Ge seeds and Ge NWs (Figure 2i and Figure S5, Supporting Information).^[59–61]

To gauge the performance of control Cu and Cu-Ge as CCs for Li metal anode, CE testing was conducted by assembling the substrates versus Li metal. The voltage – specific capacity profile (Figure S6a, Supporting Information) and corresponding differential capacity plots (Figure S6b, Supporting Information) of Cu-Ge substrate cycled between 0.011–1 V shows the characteristic lithiation–delithiation profiles of Ge NWs. Typically, the Ge lithiation occurred at 0.37 and 0.17 V, while delithiation occurred around 0.45–0.52 V. During the charging process, Li plating begins below 0 V, and this electrochemical response can be used to calculate the nucleation overpotential. Nucleation overpotential is defined as the difference between the sharp tip voltage and the voltage at the plateau.^[38,62] The nucleation overpotential for Li plating on Cu was measured to be 40 mV, while the nucleation overpotential for Li plating on Cu-Ge substrate was just 10 mV – four times lower than that of Cu (Figure 3a). The high nucleation overpotential in lithiophobic Cu tends to be the cause of uneven nucleation and growth of Li dendrites during the plating process.^[8,37] In contrast, the initial lithiation of Ge NWs in the Cu-Ge substrate forms a Li-rich lithiophilic $\text{Li}_{15}\text{Ge}_4$ phase, which decreases the nucleation overpotential

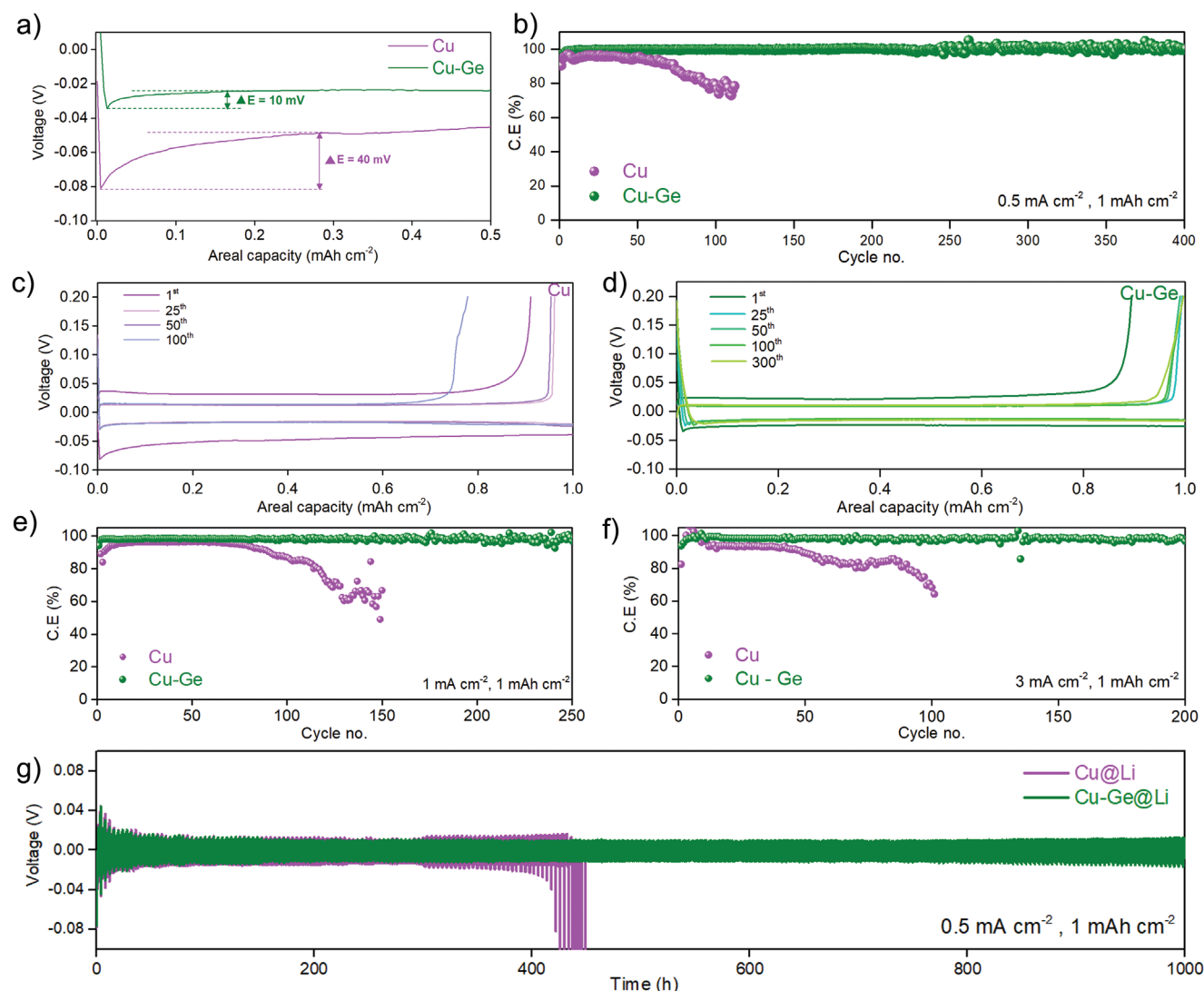


Figure 3. a) Nucleation potential of Cu and Cu-Ge at a current density of 0.5 mA cm^{-2} . b) CE test of Cu and Cu-Ge at a current density of 0.5 mA cm^{-2} and an areal capacity of 1 mAh cm^{-2} . Corresponding Voltage – Areal capacity plot of c) Cu and d) Cu-Ge at various cycle no. CE test of Cu and Cu-Ge at high current densities of e) 1 mA cm^{-2} and f) 3 mA cm^{-2} with a fixed areal capacity of 1 mAh cm^{-2} . g) Symmetric cell testing of Cu@Li || Li and Cu-Ge@Li || Li at 0.5 mA cm^{-2} at an areal capacity of 1 mAh cm^{-2} .

during subsequent Li plating below 0 V. This decrease in nucleation overpotential of Li on the Cu-Ge substrate, therefore, promotes uniform Li deposition and growth.^[63] Since Li has a high Li-ion diffusion coefficient in Ge ($6.25 \times 10^{-12} \text{ cm}^2 \text{ s}^{-1}$),^[46] the Li ions preferentially alloy with Ge, forming the $\text{Li}_{15}\text{Ge}_4$ phase. Additionally, the high Li-ion diffusion coefficient in Ge results in improved electrochemical diffusion kinetics, thereby promoting homogeneous Li-ion flux.^[64,65] This leads to a reduced Li nucleation overpotential during Li plating, as compared to lithiophobic Cu foil, where no alloying is possible between Li and Cu to guide Li deposition. Additionally, the high surface area of NW morphology (as compared to planar substrates) is also beneficial in reducing the local current density, thereby promoting uniform Li-ion flux and uniform Li deposition.^[48,66] On the contrary, the planar foils during Li deposition have non-uniform localized current density due to unstable SEI formation during the plating/stripping process which promotes

non-uniform Li deposition. When tested at 0.5 mA cm^{-2} current density for an areal capacity of 1 mAh cm^{-2} , the CE of Cu (Figure 3b) quickly decreased to 79% over 100 cycles which suggest unstable SEI formation and active material loss over the course of cycling.^[34,67,68] The Cu-Ge on the other hand exhibited a high average CE of 99.2% over 400 cycles, attributed to stable SEI formation due to regulated Li deposition/stripping on lithiophilic Cu-Ge surface. The CE fluctuations noticed during cycling could be due to the temperature fluctuations ($22 \text{ }^\circ\text{C} \pm 4$) in the lab which may have an impact on the Li-ion diffusivity through the SEI layer, thereby affecting the CE of the cell.^[69,70] The corresponding voltage-areal capacity graphs of Cu (Figure 3c) suggests higher overpotential (85 mV) in the initial cycle with a subsequent decrease in the CE as evident from the stripping curve at the 100th cycle. With Cu-Ge (Figure 3d), a much-reduced overpotential (44 mV) in the initial cycle was observed while maintaining high CE in the subsequent cycles

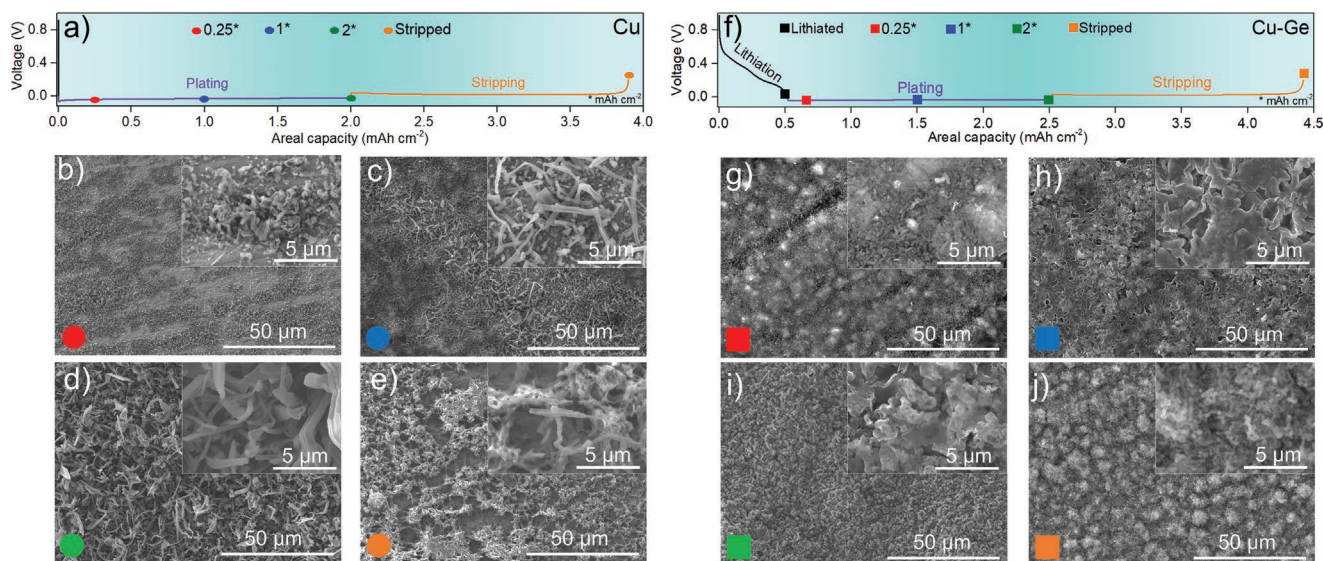


Figure 4. a) Typical voltage–areal capacity profile of Cu@Li depicting 2 mAh cm⁻² Li plating followed by complete Li stripping. SEM images of Li plating at b) 0.25, c) 1, and d) 2 mAh cm⁻² and e) stripped up to 0.2 V on Cu substrate. f) Typical voltage–areal capacity profile of Cu-Ge@Li depicting 2 mAh cm⁻² Li plating followed by complete Li stripping. SEM images of at g) 0.25, h) 1, and i) 2 mAh cm⁻² and j) stripped up to 0.2 V on Cu-Ge substrate.

(up to 300 cycles) as seen in the plating/stripping voltage–areal capacity profile of Cu-Ge. Further CE testing at a higher current density of 1 mA cm⁻² (Figure 3e) and 3 mA cm⁻² (Figure 3f) delivered high average CE values of 99.0% and 98.9% respectively after long-term cycling for Cu-Ge as compared to 86% and 88% respectively, for Cu. The CE testing at higher areal capacity (1 mA cm⁻² and 2 mAh cm⁻²) and higher current density (2 mA cm⁻² and 2 mAh cm⁻²) is given in Figure S7a,b, Supporting Information. Finally, symmetric cell testing of Cu@Li and Cu-Ge@Li performed at 0.5 mA cm⁻² for 1 mAh cm⁻² areal capacity revealed stable plating/stripping cycling of Cu-Ge@Li up to 1000 h, while Cu@Li failed quickly around 400 h with unstable cycling. Overall, CE tests and symmetric cell testing sheds light on the benefits of Ge NW grown on Cu foil (Cu-Ge), compared to planar Cu.

To visualize the electrochemical plating/stripping behavior of Li, various amounts of Li metal (mAh cm⁻²) were deposited on Cu and Cu-Ge substrates. The Li plating for Cu and Cu-Ge was studied at 0.25, 1, and 2 mAh cm⁻² before completely stripping the Li metal (Figure 4a,f). SEM analysis of Li deposited on the Cu substrate at a plating capacity of 0.25 mAh cm⁻² (Figure 4b) reveals the formation of a non-uniform, small dendritic Li island, with an obvious difference to planar Cu foil (Figure S8a, Supporting Information). At 1 mAh cm⁻² Li plating (Figure 4c), large Li dendrites are clearly seen covering the Cu substrate, with even denser coverage observed at 2 mAh cm⁻² plated Li (Figure 4d). These large dendrites are the major reason for separator piercing and short circuits, causing battery fires. After complete Li stripping (Figure 4e), remnants of Li metal with dendrites can be clearly seen on the Cu surface. The leftover “dead Li” on the Cu substrate results in active material loss during cycling and therefore is a major cause of CE losses during cycling.

When a Cu-Ge substrate was lithiated down to 0.01 V, the lithiated Ge NWs appear swollen with an average diameter of

179 nm (Figures S8b and S9, Supporting Information). Further Li plating of 0.25 mAh cm⁻² below 0 V shows the onset of uniform Li deposition on the Li₁₅Ge₄ NWs while the outline of the NW morphology is still visible (Figure 4g). It is noteworthy that no Li dendrites or non-uniform Li clusters were seen on the Cu-Ge substrate (at 0.25 mAh cm⁻² plated Li) as compared to the Cu substrate (Figure 4b). This is consistent with the highly lithiophilic nature of the Ge NWs and the reduced localized current density due to the high surface of the NW structure. Further increasing the plating capacity to 1 mAh cm⁻² (Figure 4h) and 2 mAh cm⁻² (Figure 4i), shows planar Li morphology uniformly covering the NWs with no dendrite formation. The cross-sectional SEM image of plated Li shows clear a distinction between the Cu foil and the Cu-Ge surface with uniform Li plating (Figure S10, Supporting Information). XRD analysis of the Cu@Li and Cu-Ge@Li samples with 2 mAh cm⁻² Li plated confirms the presence of metallic Li in both samples (Figure S11, Supporting Information). The Cu-Ge@Li sample additionally confirms the complete alloying of Ge NWs to Li₁₅Ge₄ NWs. Once Li is fully stripped from the Cu-Ge@Li anode, the NW morphology is clearly visible with no visible remains of Li deposits on the NW surface (Figure 4j). This suggests that the lithiophilic surface not only promotes uniform Li deposition but also helps maintain good electrical contact between the Li and Cu-Ge substrate, resulting in complete Li stripping. The EDX analysis performed on Cu-Ge substrate at various plating stages shows a uniform weakening of the Ge signals as the plating capacity increases. This qualitatively suggests that Li uniformly covers the entire Cu-Ge surface (Figure S12, Supporting Information). Once all the Li was stripped, Ge signals once again became intense and uniform, suggesting complete Li stripping. Moreover, SEM analysis of Cu-Ge substrate after 50 Li plating/stripping cycles showed that the Ge NW morphology was still maintained, confirming Cu-Ge role as a robust current collector for Li metal anodes (Figure S13, Supporting Information).

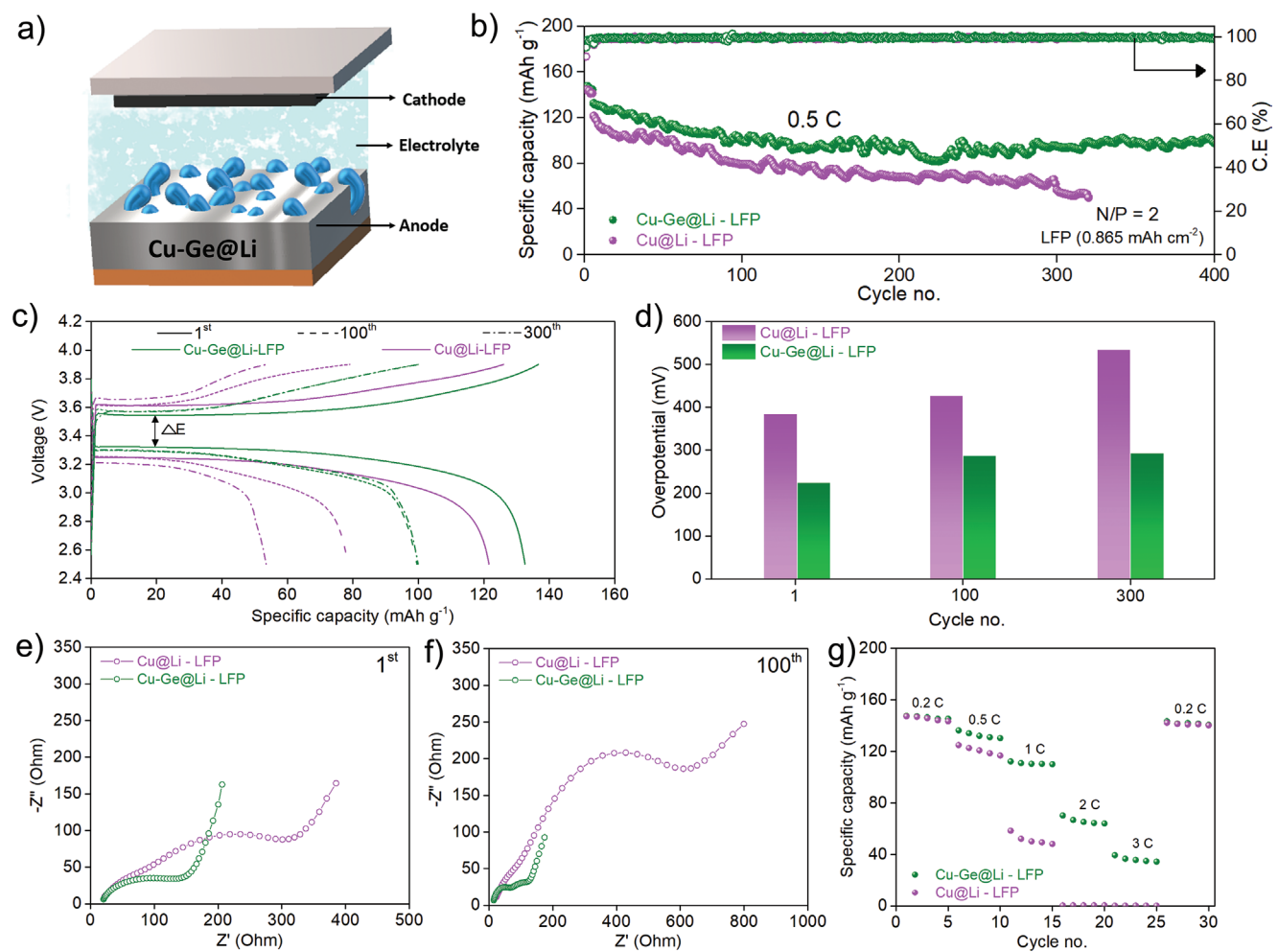


Figure 5. a) Schematic illustration of a Li metal anode full cell consisting of the cathode, electrolyte, and Cu-Ge@Li anode. b) Cyclic performance of Cu@Li-LFP and Cu-Ge@Li-LFP full cells at 0.5 C with controlled N/P = 2. c) Corresponding voltage – specific capacity plot and d) overpotential versus cycle no. at various cycles. EIS after e) 1st and f) 100th cycles. g) Rate capability test of Cu@Li-LFP and Cu-Ge@Li-LFP at various C-rates.

To substantiate the benefits derived from the innovative Cu-Ge substrate architecture, extensive full-cell testing was conducted by assembling Cu@Li and Cu-Ge@Li substrates against various cathode systems (i.e., LFP, NMC, and S) in a coin cell setup (Figure 5a). Li was plated on the Cu and Cu-Ge substrates, with the amount of Li plated corresponding to an N/P ratio of 2.0. Cu@Li and Cu-Ge@Li were first matched with LFP cathodes (areal capacity 0.87 mAh cm⁻²) and cycled at 0.5 C (Figure 5b). The cycling data shows that a high initial specific capacity of 130 mAh g⁻¹ from the Cu-Ge@Li-LFP cell was obtained, compared to 120 mAh g⁻¹ from the Cu@Li-LFP cell. The Cu-Ge@Li-LFP cell delivered a specific capacity of 100 mAh g⁻¹ after 400 cycles with a capacity retention of 76%, whereas the Cu@Li-LFP cell delivered a specific capacity of 50 mAh g⁻¹ after 320 cycles with a low capacity retention of only 42%. A comparison of the voltage-specific capacity graph of Cu@Li-LFP and Cu-Ge@Li-LFP at the 1st, 100th, and 300th cycles shows a typical charge-discharge profile, with noticeable overpotential difference among the two metal anode substrates (Figure 5c). The Cu@Li-LFP shows high overpotential of 385, 430, and 535 mV while the Cu-Ge@Li-LFP cell showed much

lower overpotential of 225, 285, and 290 mV after 1st, 100th, and 300th cycle respectively (Figure 5d). The improved performance of the Cu-Ge@Li-LFP cell was further investigated by performing electrochemical impedance spectroscopy (EIS) analysis. EIS analysis shows high R_{SEI} and R_{ct} for the Cu@Li-LFP cell (112.3 and 176.8 Ohm), which is significantly higher than for the Cu-Ge@Li-LFP cell (28.84 and 123 Ohm) after the 1st cycle (Figure 5e, Figure S14 and Table S1, Supporting Information). The R_{SEI} and R_{ct} further increased to 125.6 and 422.7 Ohm in the Cu@Li-LFP cell after 100 cycles (Figure 5f), suggesting excessive electrolyte decomposition and an unstable SEI formation, causing high overpotentials and capacity loss during electrochemical cycling.^[71,72] In stark contrast, the R_{SEI} and R_{ct} of Cu-Ge@Li-LFP cell were 30.3 and 55.71 Ohm respectively. The decrease in the cell resistance again signifies the stable SEI formation on the Cu-Ge@Li anode, minimizing electrolyte decomposition and capacity loss during the cycling process. Finally, the rate capability test was performed to demonstrate the cyclic performance of the Cu-Ge@Li anode at high C-rates (Figure 5g). The rate-capability test clearly shows that Cu-Ge@Li-LFP cell delivered 148, 136, 112, 70, and 40 mAh g⁻¹

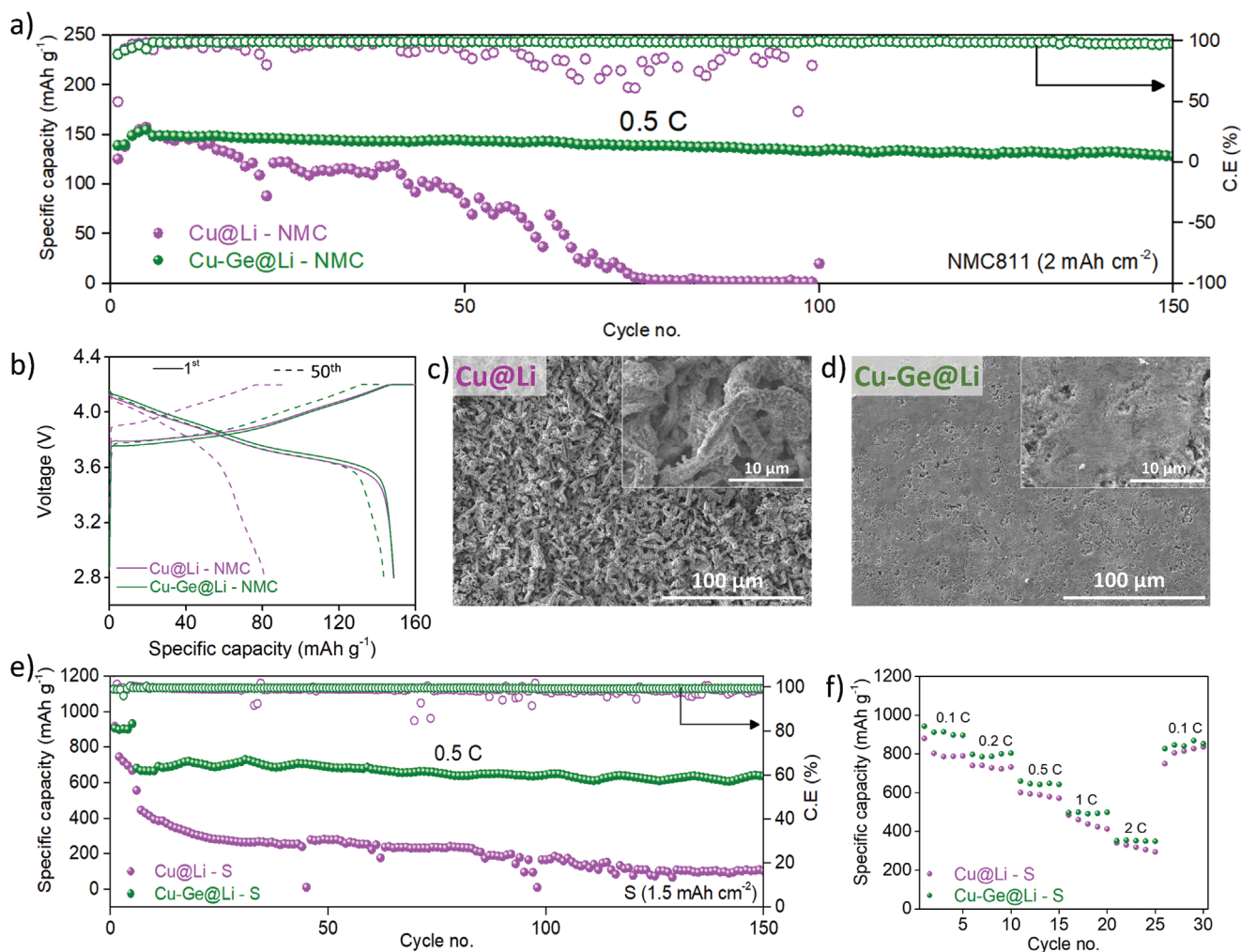


Figure 6. a) Cyclic performance of Cu@Li-NMC811 and Cu-Ge@Li-NMC811 full cells at 0.5 C with controlled N/P = 2. b) Corresponding voltage – specific capacity plot after 1st and 50th cycles. SEM images of c) Cu@Li and d) Cu-Ge@Li anodes after 100 cycles. e) Cyclic performance of Cu@Li-S and Cu-Ge@Li-S full cells at 0.5 C. f) Corresponding rate capability test of Cu@Li-S and Cu-Ge@Li-S at various C-rates.

at 0.2, 0.5, 1, 2, and 3 C respectively. In comparison, Cu@Li-LFP delivered much lower specific capacities with cell failure after 1 C. The corresponding specific capacity–voltage of the Cu@Li-LFP cell shows much higher overpotentials at similar C-rates as compared to the Cu-Ge@Li-LFP cell (Figure S15, Supporting Information).

To improve the ED of LMBs, high-capacity cathodes with minimal Li source (low N/P ratios) would be a beneficial step towards achieving practical applications of LMBs.^[7,73] Therefore, high loading (10.79 mg cm⁻²) and high areal capacity NMC811 (2 mAh cm⁻²) was tested against Cu@Li and Cu-Ge@Li while maintaining a low N/P ratio of 2.0 (Figure 6a). The electrochemical data clearly show that the Cu-Ge@Li-NMC cell outperformed the Cu@Li-NMC cell. The specific capacity increase in both Cu@Li-NMC and Cu-Ge@Li-NMC cells during initial cycling could be associated with the activation of NMC cathode material.^[74,75] The Cu-Ge@Li-NMC cell achieved an initial capacity of 148 mAh g⁻¹ at 0.5 C, with capacity retention and an average CE of 86.5% and 99.2% respectively. However, while the Cu@Li-NMC cell delivered a similar initial specific capacity

(148 mAh g⁻¹) at 0.5 C, the specific capacity quickly dropped to zero in less than 100 cycles, with massive fluctuations in the CE. The corresponding voltage-specific capacity graph shows a stable electrochemical response in Cu-Ge@Li-NMC during the 1st and 50th cycles whereas capacity drop with high overpotentials can be clearly observed in the voltage profiles of the Cu@Li-NMC cell (Figure 6b). SEM analysis conducted post-cycling on Cu@Li shows uneven Li deposition with massive dendrite formation (Figure 6c), which explains the poor cycling stability and cell failure. In contrast, the Cu-Ge@Li shows uniform deposition across the anode surface with no dendrite formation, therefore promoting stable cycling performance even with this high areal capacity cathode system (Figure 6d). The Cu-Ge@Li anode (when paired with the NMC811 cathode) represents an impressive 63.6% mass reduction compared to a state-of-the-art graphite-based anode (Table S2, Supporting Information), which demonstrates the significant potential for ED enhancement based on this anode architecture.

The Cu-Ge@Li anode was further tested against a sulfur cathode (1.55 mAh cm⁻², Figure S16, Supporting Information)

to show its compatibility with different types of cathode systems (Figure 6e). The electrochemical cycling shows a massive drop in the specific capacity of Cu@Li-S from 560 to 100 mAh g⁻¹ after 150 cycles, with a capacity retention of 18%. In contrast, Cu-Ge@Li-S shows high specific capacity (initial- 683 mAh g⁻¹, final- 635 mAh g⁻¹), with remarkable capacity retention of 93% after 150 cycles. This again highlights the reversible Li plating/stripping performance of the Cu-Ge substrate as compared to Cu highlighted earlier during CE testing of the two substrates (Figure 3). The corresponding voltage-specific capacity profiles show similar trends of high overpotentials using Cu@Li as compared to Cu-Ge@Li anode with increasing no. of cycles (Figure S17, Supporting Information). Finally, the rate capability test performed confirms a similar trend with Cu-Ge@Li-S outperforming the Cu@Li-S cell when tested at various C-rates (0.1–2 C) (Figure 6f).

3. Conclusion

We report the conversion of the lithiophobic surface of Cu current collectors to a highly lithiophilic Cu-Ge CC via the rapid VSS growth of Ge NWs. In comparison to planar Cu substrates, the Cu-Ge substrates provide lithiophilic anchoring points, enabling the Cu-Ge to function as high-performance CCs for LMBs. The benefits derived from using the Cu-Ge substrate resulted in lower nucleation overpotentials (4 times lower than planar Cu) during Li plating, with high CE during plating/stripping cycling at various combinations of current densities (0.5, 1, 2, and 3 mA cm⁻²) and plating capacities (1 and 2 mAh cm⁻²). When cycled as practical LMBs using controlled Li plating (on Cu and Cu-Ge substrates) against LFP, NMC and S cathodes, the Cu-Ge substrate demonstrated fast charge kinetics and high reversibility during cycling. The approach is an important step towards practical LMBs, required for the next step in high ED battery development.

4. Experimental Section

Synthesis of Ge NWs on Cu Foil: Commercial dendritic Cu foil (Schlenk, 18–20 μm thickness) was washed three times with isopropanol and acetone before vacuum drying in an oven overnight. To grow Ge NWs, a previously reported protocol was followed.^[53] Briefly, Cu foil was heated up to 450 °C on a hot plate followed by injection of Diphenylgermane (DPG, 10 μl) using a heat condenser. The reaction was allowed to proceed for 5 min before the heat condenser was removed and Ge-grown Cu foil (Cu-Ge) was removed from the hot plate to cool it down. All the above procedure was carried out in an Ar-filled glove box. The Cu-Ge samples were washed with toluene and dried under air overnight before further use.

Material Characterization: XRD analysis was conducted using a Panalytical Empyrean instrument fitted with a Cu K_α source (λ = 1.5418 Å) and an X'celerator detector. For air-sensitive samples, a protective polymer film along with an XRD holder for air-sensitive samples was used to prevent oxidation. SEM and EDS analysis were conducted on a Hitachi SU-70 instrument. The SEM was operated at 20 kV for the analysis of Cu and Cu-Ge samples or at 5 kV for Li-containing samples to avoid sample degradation. For post-cycling SEM analysis of deposited Li, the substrates were extracted, washed with dimethoxy ethane (DME) solvent, and dried in an Ar-filled glove box before transferring into SEM without air exposure. Transmission electron microscopy (TEM) was conducted using Aberration-corrected TEM (Titan/Krios) operated at 300 kV, also fitted with a Bruker Super X detector. For TEM analysis,

the Cu-Ge sample was ultrasonicated in ethanol for 2 min and drop-casted on a lacey carbon Ni grid for TEM analysis. X-ray photoelectron spectroscopy (XPS) was conducted using a Kratos AXIS ULTRA spectrometer fitted with a mono Al K (1486.58 eV) X-ray gun. Calibration was conducted using C 1s line at 284.8 eV with construction and peak fitting was performed using Casa XPS software.

Electrochemical Characterization: All electrochemical characterization was conducted by assembling CR2032 coin cells in an Ar-filled glove box with O₂ and H₂O levels kept below 1 ppm. The symmetric cell and half-cell testing along with electrochemical impedance spectroscopy was conducted using either a Neware battery cycler or a Biologic instrument. The electrolyte used was 1 M LiTFSI (DOL: DME, 1:1, vol. %) + 0.25 M LiNO₃ along with Celgard 2325 separator. All the cells were cycled at ambient lab conditions. For CE tests, Cu and Cu-Ge substrates assembled against Li foil were cycled between 0.011–1 V for five cycles at low current (to remove surface contaminations), before switching to plating (at various current densities and plating capacities) and stripping up to 0.2 V to ensure all plated Li had been stripped out. For symmetric cell testing, 5 mAh cm⁻² Li was pre-deposited on Cu and Cu-Ge substrates before cycling at various current densities and areal capacities. For LFP (LiFePO₄) cathode, 80% LFP, 10% carbon black (CB), and 10% PVDF were mixed in NMP solvent before casting it on Al foil, followed by overnight vacuum drying at 70 °C. The corresponding LFP loading was 5–5.5 mg cm⁻² (areal capacity: 0.875 mAh cm⁻²) and the cathodes were cycled between 2.5–3.9 V. The NMC811 cathode was procured from NEI Corporation with nominal mass loading of 10.79 mg cm⁻² and an areal capacity of 2 mAh cm⁻². For high-loading NMC811, 1 M LiPF₆ (EC: DEC) + 10% FEC electrolyte (with a volume of 80 μl) was used to avoid electrolyte degradation in the tested voltage window (2.8–4.2 V). Additionally, a CCCV step was also added during electrochemical cycling. For S cathodes, a carbon-sulfur composite (C70S) was prepared by heat-melting the carbon black–S mixture (CB:S, 30:70, wt.%) at 155 °C for 12 h in a sealed vessel. The slurry composed of 70% C70S, 15% CB, and 15% PVDF was mixed using NMP solvent and casted on an Al foil before drying overnight in a vacuum oven at 70 °C. The corresponding mass loading of active S was 1.5 mg cm⁻². 1 M LiTFSI (DOL: DME, 1:1, v/v) + 0.25 M LiNO₃ was used to test sulfur cathodes with a fixed amount of 45 μl in all the cells. All full cells were pre-cycled at 0.1 C for 5 cycles before testing at 0.5 C. For Li-metal full-cell testing, Li was pre-deposited on Cu and Cu-Ge foils to correspond to an N/P ratio of 2.0. The N/P ratio corresponds to the areal capacity of deposited Li over the areal capacity of the cathode being tested.

Supporting Information

Supporting Information is available from the Wiley Online Library or from the author.

Acknowledgements

This project was supported by Science Foundation Ireland under grant no. 18/SIRG/5484. The authors would also like to thank Dr. Fathima Laffir (XPS instrument scientist - Bernal Institute) for help with XPS analysis.

Open access funding provided by IReL.

Conflict of Interest

The authors declare no conflict of interest.

Data Availability Statement

The data that support the findings of this study are available from the corresponding author upon reasonable request.

Keywords

binder-free, current collectors, energy density, Li metal anodes, nanowires

Received: December 19, 2022
Revised: January 16, 2023
Published online:

- [1] J. W. Choi, D. Aurbach, *Nat. Rev. Mater.* **2016**, *1*, 16013.
[2] S. Chu, Y. Cui, N. Liu, *Nat. Mater.* **2016**, *16*, 16.
[3] A. Eftekhari, *ACS Sustainable Chem. Eng.* **2019**, *7*, 3684.
[4] J. B. Goodenough, Y. Kim, *Chem. Mater.* **2010**, *22*, 587.
[5] X. Shen, X.-Q. Zhang, F. Ding, J.-Q. Huang, R. Xu, X. Chen, C. Yan, F.-Y. Su, C.-M. Chen, X. Liu, Q. Zhang, *Energy Mater. Adv.* **2021**, *2021*, 1.
[6] D. Lin, Y. Liu, Y. Cui, *Nat. Nanotechnol.* **2017**, *12*, 194.
[7] P. Albertus, S. Babinec, S. Litzelman, A. Newman, *Nat. Energy* **2018**, *3*, 16.
[8] X. B. Cheng, R. Zhang, C. Z. Zhao, Q. Zhang, *Chem. Rev.* **2017**, *117*, 10403.
[9] J. Wang, J. Zheng, X. Liu, *Phys. Chem. Chem. Phys.* **2022**, 17920.
[10] T. Liu, J. P. Vivek, E. W. Zhao, J. Lei, N. Garcia-Araez, C. P. Grey, *Chem. Rev.* **2020**, *120*, 6558.
[11] F. Wu, G. Yushin, *Energy Environ. Sci.* **2017**, *10*, 435.
[12] Q. Wang, B. Liu, Y. Shen, J. Wu, Z. Zhao, C. Zhong, W. Hu, *Adv. Sci.* **2021**, *8*, 1.
[13] Y. Zhang, T. T. Zuo, J. Popovic, K. Lim, Y. X. Yin, J. Maier, Y. G. Guo, *Mater. Today* **2020**, *33*, 56.
[14] H. Kim, G. Jeong, Y. U. Kim, J. H. Kim, C. M. Park, H. J. Sohn, *Chem. Soc. Rev.* **2013**, *42*, 9011.
[15] J. Xiang, L. Yang, L. Yuan, K. Yuan, Y. Zhang, Y. Huang, J. Lin, F. Pan, Y. Huang, *Joule* **2019**, *3*, 2334.
[16] Y. Gao, T. Rojas, K. Wang, S. Liu, D. Wang, T. Chen, H. Wang, A. T. Ngo, D. Wang, *Nat. Energy* **2020**, *5*, 534.
[17] S. Liu, X. Ji, N. Piao, J. Chen, N. Eidson, J. Xu, P. Wang, L. Chen, J. Zhang, T. Deng, S. Hou, T. Jin, H. Wan, J. Li, J. Tu, C. Wang, *Angew. Chem., Int. Ed.* **2021**, *60*, 3661.
[18] Y. Guo, H. Li, T. Zhai, *Adv. Mater.* **2017**, *29*, 1700007.
[19] W. Xu, J. Wang, F. Ding, X. Chen, E. Nasybulin, Y. Zhang, J. G. Zhang, *Energy Environ. Sci.* **2014**, *7*, 513.
[20] S. A. Gavrilov, A. A. Dronov, I. M. Gavrilin, R. L. Volkov, N. I. Borgardt, A. Y. Trifonov, A. V. Pavlikov, P. A. Forsh, P. K. Kashkarov, *J. Raman Spectrosc.* **2018**, *49*, 810.
[21] P. Xiao, R. Luo, Z. Piao, C. Li, J. Wang, K. Yu, G. Zhou, H. M. Cheng, *ACS Energy Lett.* **2021**, *6*, 3170.
[22] J. Zheng, M. H. Engelhard, D. Mei, S. Jiao, B. J. Polzin, J. G. Zhang, W. Xu, *Nat. Energy* **2017**, *2*, 17012.
[23] K. Xu, *Chem. Rev.* **2004**, *104*, 4303.
[24] J. Zheng, J. A. Lochala, A. Kwok, Z. D. Deng, J. Xiao, *Adv. Sci.* **2017**, *4*, 1.
[25] G. A. Giffin, *Nat. Commun.* **2022**, *13*, 5250.
[26] W. Z. Huang, C. Z. Zhao, P. Wu, H. Yuan, W. E. Feng, Z. Y. Liu, Y. Lu, S. Sun, Z. H. Fu, J. K. Hu, S. J. Yang, J. Q. Huang, Q. Zhang, *Adv. Energy Mater.* **2022**, *12*, 2201044.
[27] Q. Zhao, S. Stalin, C. Z. Zhao, L. A. Archer, *Nat. Rev. Mater.* **2020**, *5*, 229.
[28] H. Ye, S. Xin, Y. X. Yin, J. Y. Li, Y. G. Guo, L. J. Wan, *J. Am. Chem. Soc.* **2017**, *139*, 5916.
[29] K. Lin, X. Xu, X. Qin, G. Zhang, M. Liu, F. Lv, Y. Xia, F. Kang, G. Chen, B. Li, *Energy Storage Mater.* **2020**, *26*, 250.
[30] Y. Zhao, Q. Li, Z. Liu, L. Fan, J. Li, Z. Ma, X. Qin, G. Shao, *ACS Appl. Mater. Interfaces* **2020**, *12*, 37967.
[31] P. Zhai, Y. Wei, J. Xiao, W. Liu, J. Zuo, X. Gu, W. Yang, S. Cui, B. Li, S. Yang, Y. Gong, *Adv. Energy Mater.* **2020**, *10*, 1903339.
[32] S. Lu, Z. Wang, H. Yan, R. Wang, K. Lu, Y. Cheng, W. Qin, X. Wu, *J. Energy Chem.* **2020**, *41*, 87.
[33] D. Zhang, A. Dai, M. Wu, K. Shen, T. Xiao, G. Hou, J. Lu, Y. Tang, *ACS Energy Lett.* **2020**, *5*, 180.
[34] J. Pu, J. Li, K. Zhang, T. Zhang, C. Li, H. Ma, J. Zhu, P. v. Braun, J. Lu, H. Zhang, *Nat. Commun.* **2019**, *10*, 1896.
[35] P. Zhu, D. Gastol, J. Marshall, R. Sommerville, V. Goodship, E. Kendrick, *J. Power Sources* **2021**, *485*, 229321.
[36] H. C. Chu, H. Y. Tuan, *J. Power Sources* **2017**, *346*, 40.
[37] Y. Liu, D. Gao, H. Xiang, X. Feng, Y. Yu, *Energy Fuels* **2021**, *35*, 12921.
[38] K. Yan, Z. Lu, H. W. Lee, F. Xiong, P. C. Hsu, Y. Li, J. Zhao, S. Chu, Y. Cui, *Nat. Energy* **2016**, *1*, 16010.
[39] G. Wang, X. Xiong, P. Zou, X. Fu, Z. Lin, Y. Li, Y. Liu, C. Yang, M. Liu, *Chem. Eng. J.* **2019**, *378*, 122243.
[40] S. Cui, P. Zhai, W. Yang, Y. Wei, J. Xiao, L. Deng, Y. Gong, *Small* **2020**, *16*, 1.
[41] Q. Zhang, J. Luan, Y. Tang, X. Ji, S. Wang, H. Wang, *J. Mater. Chem. A* **2018**, *6*, 18444.
[42] A. A. Assegie, C. C. Chung, M. C. Tsai, W. N. Su, C. W. Chen, B. J. Hwang, *Nanoscale* **2019**, *11*, 2710.
[43] W. Lu, C. Wu, W. Wei, J. Ma, L. Chen, Y. Chen, *J. Mater. Chem. A* **2019**, *7*, 24262.
[44] C. Chou, H. Kim, G. S. Hwang, *J. Phys. Chem. C* **2011**, *115*, 20018.
[45] J. Zhao, J. Sun, A. Pei, G. Zhou, K. Yan, Y. Liu, D. Lin, Y. Cui, *Energy Storage Mater.* **2018**, *10*, 275.
[46] P. R. Abel, A. M. Chockla, Y. M. Lin, V. C. Holmberg, J. T. Harris, B. A. Korgel, A. Heller, C. B. Mullins, *ACS Nano* **2013**, *7*, 2249.
[47] C. S. Fuller, J. C. Severiens, *Phys. Rev.* **1954**, *96*, 1322.
[48] L. L. Lu, J. Ge, J. N. Yang, S. M. Chen, H. bin Yao, F. Zhou, S. H. Yu, *Nano Lett.* **2016**, *16*, 4431.
[49] C. P. Yang, Y. X. Yin, S. F. Zhang, N. W. Li, Y. G. Guo, *Nat. Commun.* **2015**, *6*, 8058.
[50] S. Abdul Ahad, S. Bhattacharya, S. Kilian, M. Ottaviani, K. M. Ryan, T. Kennedy, D. Thompson, H. Geaney, *Small* **2023**, *19*, 2205142.
[51] E. Mullane, T. Kennedy, H. Geaney, K. M. Ryan, *ACS Appl. Mater. Interfaces* **2014**, *6*, 18800.
[52] C. A. Barrett, H. Geaney, R. D. Gunning, F. R. Laffir, K. M. Ryan, *Chem. Commun.* **2011**, *47*, 3843.
[53] H. Geaney, G. Bree, K. Stokes, G. A. Collins, I. S. Aminu, T. Kennedy, K. M. Ryan, *Chem. Commun.* **2019**, *55*, 7780.
[54] D. McNulty, H. Geaney, D. Buckley, C. O'Dwyer, *Nano Energy* **2018**, *43*, 11.
[55] T. Kennedy, E. Mullane, H. Geaney, M. Osiak, C. O'Dwyer, K. M. Ryan, *Nano Lett.* **2014**, *14*, 716.
[56] H. Geaney, E. Mullane, K. M. Ryan, *J. Mater. Chem. C* **2013**, *1*, 4996.
[57] H. Geaney, C. Dickinson, C. A. Barrett, K. M. Ryan, *Chem. Mater.* **2011**, *23*, 4838.
[58] C. S. Fuller, J. D. Struthers, J. A. Ditzenberger, K. B. Wolfstirn, *Phys. Rev.* **1954**, *93*, 1182.
[59] C. Shang, L. Hu, D. Luo, K. Kempa, Y. Zhang, G. Zhou, X. Wang, Z. Chen, *Adv. Sci.* **2020**, *7*, 1.
[60] C. Zhang, F. Chai, L. Fu, P. Hu, S. Pang, G. Cui, *J. Mater. Chem. A* **2015**, *3*, 22552.
[61] J. Liang, X. Li, Z. Hou, J. Jiang, L. Hu, W. Zhang, Y. Zhu, Y. Qian, *Small* **2016**, *12*, 6024.
[62] P. Biswal, S. Stalin, A. Kludze, S. Choudhury, L. A. Archer, *Nano Lett.* **2019**, *19*, 8191.
[63] D. Lin, Y. Liu, Z. Liang, H. W. Lee, J. Sun, H. Wang, K. Yan, J. Xie, Y. Cui, *Nat. Nanotechnol.* **2016**, *11*, 626.

- [64] C. Wei, Y. Zhang, Y. Tian, L. Tan, Y. An, Y. Qian, B. Xi, S. Xiong, J. Feng, Y. Qian, *Energy Storage Mater.* **2021**, *38*, 157.
- [65] C. Wei, L. Tan, Y. Tao, Y. An, Y. Tian, H. Jiang, J. Feng, Y. Qian, *Energy Storage Mater.* **2021**, *34*, 12.
- [66] H. Ye, Z. J. Zheng, H. R. Yao, S. C. Liu, T. T. Zuo, X. W. Wu, Y. X. Yin, N. W. Li, J. J. Gu, F. F. Cao, Y. G. Guo, *Angew. Chem., Int. Ed.* **2019**, *58*, 1094.
- [67] Y. Sun, C. Zhao, K. R. Adair, Y. Zhao, L. v. Goncharova, J. Liang, C. Wang, J. Li, R. Li, M. Cai, T. K. Sham, X. Sun, *Energy Environ. Sci.* **2021**, *14*, 4085.
- [68] H. Zhang, X. Liao, Y. Guan, Y. Xiang, M. Li, W. Zhang, X. Zhu, H. Ming, L. Lu, J. Qiu, Y. Huang, G. Cao, Y. Yang, L. Mai, Y. Zhao, H. Zhang, *Nat. Commun.* **2018**, *9*, 1.
- [69] T. Kennedy, M. Brandon, F. Laffir, K. M. Ryan, *J. Power Sources* **2017**, *359*, 601.
- [70] S. Kilian, K. McCarthy, K. Stokes, T. Esther Adegoke, M. Conroy, I. Saana Amiin, H. Geaney, T. Kennedy, K. M. Ryan, *Small* **2021**, *17*, 2005443.
- [71] K. Yan, H. W. Lee, T. Gao, G. Zheng, H. Yao, H. Wang, Z. Lu, Y. Zhou, Z. Liang, Z. Liu, S. Chu, Y. Cui, *Nano Lett.* **2014**, *14*, 6016.
- [72] Y. Zhang, B. Liu, E. Hitz, W. Luo, Y. Yao, Y. Li, J. Dai, C. Chen, Y. Wang, C. Yang, H. Li, L. Hu, *Nano Res.* **2017**, *10*, 1356.
- [73] C. Niu, H. Pan, W. Xu, J. Xiao, J. G. Zhang, L. Luo, C. Wang, D. Mei, J. Meng, X. Wang, Z. Liu, L. Mai, J. Liu, *Nat. Nanotechnol.* **2019**, *14*, 594.
- [74] S. Y. Luchkin, M. A. Kirsanova, D. A. Aksyonov, S. A. Lipovskikh, V. A. Nikitina, A. M. Abakumov, K. J. Stevenson, *ACS Appl. Energy Mater.* **2022**, *5*, 7758.
- [75] X.-G. Sun, C. J. Jafta, S. Tan, A. Borisevich, R. B. Gupta, M. P. Paranthaman, *J. Electrochem. Soc.* **2022**, *169*, 020565.